Applied Mathematics and Computation 267 (2015) 682–697

Contents lists available at ScienceDirect

Applied Mathematics and Computation

journal homepage: www.elsevier.com/locate/amc

Anisotropic *hp*-adaptive discontinuous Galerkin method for the numerical solution of time dependent PDEs ☆

Vít Dolejší

Charles University Prague, Faculty of Mathematics and Physics, Sokolovská 83, 186 75 Praha, Czech Republic

ARTICLE INFO

Keywords:
hp-methods
Anisotropic mesh adaptation
Interpolation error estimates

ABSTRACT

We deal with the numerical solution of time dependent problems with the aid of anisotropic *hp*-grids. We present an algorithm which generates a sequence of anisotropic triangular grids and the corresponding polynomial approximation degrees in such a way that the interpolation error measured in the discrete $L^\infty(0,T;L^q(\Omega))$-norm ($q \in [1,\infty]$ and $\Omega \subset \mathbb{R}^2$) is under a given tolerance and the number of degrees of freedom is as small as possible. The efficiency of the algorithm is demonstrated by numerical experiments.

1. Introduction

An automatic mesh adaptation is an efficient tool for the numerical solution of partial differential equations (PDEs). In this paper we deal with a method which combines two approaches:

- (*isotropic*) *hp-adaptive methods*, which allow the adaptation in the element size h as well as in the polynomial degree of approximation p. Under some assumptions, they converges at an exponential rate in the number of degrees of freedom, see, e.g., [1–6] and the references cited therein.
- *anisotropic mesh adaptation* techniques, generating anisotropic elements (i.e., long and thin triangles), which are suitable in computation of problems with boundary or internal layers, see, e.g., [7–16]. These works dealt mostly with a first order approximation, thus the Hessian matrix (=matrix of the second order derivatives) is naturally employed for the definition of the Riemann metric generating the anisotropy of grids. Furthermore, in [17,18], the Riemann metrics (defining the optimal anisotropic mesh in the $W^{k,q}$-norm) were derived for the higher polynomial approximations degree (>1). Moreover, optimally adapted meshes for finite element approximations of arbitrary order in the L^q-norm and the $W^{k,q}$-norm were derived in [19,20], respectively.

In [21] we developed an adaptive technique for steady problems, which employs both these aspects, i.e., it generates the so-called *anisotropic hp-grids*, where each element is characterized by its *size*, the *orientation*, the *aspect ratio*, and the *local polynomial approximation degree*. The orientation of the anisotropic element is the direction, along which its shape is extended, the size of the element corresponds to its diameter and the aspect ratio of the element is (roughly speaking) to the ratio between the size of the element and its "width".

☆ This work was supported by Grant No. 13-00522S of the Czech Science Foundation. The author acknowledges the membership in the Nečas Center for Mathematical Modeling ncmm.karlin.mff.cuni.cz.

E-mail address: dolejsi@karlin.mff.cuni.cz

http://dx.doi.org/10.1016/j.amc.2014.12.099
0096-3003/

A *hp*-mesh can be described by two functions: $\mathcal{M}:\Omega\to Sym$ ($\Omega\subset\mathbb{R}^2$ is the computational domain and *Sym* is the space of 2×2 symmetric, positively definite matrices) and $\mathcal{P}:\Omega\to\mathbb{R}^+$ (= the set of positive real numbers). The function $\mathcal{M}$ represents the Riemann metric and thus defines a triangular grid. The function $\mathcal{P}$ defines the polynomial approximation degree on each triangle of this grid.

The algorithm developed in [21] constructs, for a given function $u:\Omega\to\mathbb{R}^2$, an anisotropic *hp*-mesh such that.

(i) the *interpolation error* of a projection of u on S_{hp} (=space of discontinuous piecewise polynomial functions uniquely defined for each *hp*-grid) in the L^q-norm ($q\in[1,\infty]$) is under a given tolerance,
(ii) the dimension of S_{hp} (=*number of degrees of freedom*) is the smallest possible.

In this paper, we extend the technique from [21] to the numerical solution of time-dependent PDEs. We develop an algorithm which generates a sequence of anisotropic *hp*-grids in such a way that the interpolation error measured in the discrete $L^\infty(0,T;L^q(\Omega))$-norm is under a given tolerance and the number of degrees of freedom is as small as possible. This algorithm involves several re-meshing after each unsuccessful time step. The algorithm generating *hp*-meshes is combined with the space–time discontinuous Galerkin method which simply deals with different grids on different time levels. Moreover, a special modification is proposed to the numerical solution of unsteady viscous compressible flows. Our technique partly generalizes the approach from [22], where the P^1-polynomial approximation is employed and applied to incompressible bi-fluid flow problems.

The content of the rest of the paper is the following. In Section 2, we introduce basic notations and properties of anisotropic *hp*-meshes. In Section 3 we recall a theoretical background of the presented *hp*-adaptation algorithm developed in [21]. Its application to steady problems is briefly given in Section 4. The main novelty of this paper is presented in Section 5, where the algorithm for the numerical solution of time dependent problems is developed. The efficiency of the algorithm is demonstrated by experiments given in Section 6. The application of this technique to the numerical solution of the compressible Navier–Stokes equations is given in Section 7. Finally, we add several concluding remarks.

2. Anisotropic *hp*-meshes

In this section we introduce a basic notation for the anisotropic *hp*-meshes. Let $\Omega\subset\mathbb{R}^2$ be a bounded computational domain with a polygonal boundary $\partial\Omega$. We denote by $\mathcal{T}_h=\{K\}$ ($h>0$) a conforming *triangulation* of Ω and by $\mathcal{F}_h$ the set of edges of $\mathcal{T}_h$. The edges $\boldsymbol{e}\in\mathcal{F}_h$ are considered as vectors from $\mathbb{R}^2$ given by its endpoints, the orientation of $\boldsymbol{e}\in\mathcal{F}_h$ is arbitrary.

2.1. Anisotropic triangle

In virtue of the papers cited above, the anisotropy of a triangle is described by a matrix $\mathbb{M}\in Sym$, where *Sym* is the space of 2×2 symmetric positively definite matrices. Let the matrix $\mathbb{M}\in Sym$ be given, it can be decomposed in the form

$$\mathbb{M}=\mathbb{Q}_{\phi_{\mathbb{M}}}^{\mathrm{T}}\mathrm{diag}(\lambda_{\mathbb{M},1},\lambda_{\mathbb{M},2})\mathbb{Q}_{\phi_{\mathbb{M}}}, \tag{1}$$

where $\mathrm{diag}(a,b)$ denotes the diagonal matrix with the entries a and b, $0<\lambda_{\mathbb{M},1}\leqslant\lambda_{\mathbb{M},2}$ are the eigenvalues of $\mathbb{M}$, $\phi_{\mathbb{M}}\in[0,\pi)$ and $\mathbb{Q}_\phi$ is the *rotation* through angle ϕ in the counter clockwise direction. Moreover, the relation

$$\Sigma_{\mathbb{M}}:=\{x\in\mathbb{R}^2;\ x^{\mathrm{T}}\mathbb{M}x\leqslant 1\}, \tag{2}$$

defines an *ellipse* whose semi-axes have lengths $r_{\mathbb{M},i}=(\lambda_{\mathbb{M},i})^{-1/2}$, $i=1,2$ and its orientation is $\phi_{\mathbb{M}}$ (=angle between the major semi-axis and the axis x_1 of the coordinate system), see Fig. 1, left.

Furthermore, let $\mathbb{M}\in Sym$ and $\Sigma_{\mathbb{M}}$ be the ellipse given by (2). Let $K_{\mathbb{M}}$ be an acute-angle isosceles triangle which is inscribed into the ellipse $\Sigma_{\mathbb{M}}$ and which has the maximal possible area, see Fig. 1, left. We call $K_{\mathbb{M}}$ the *anisotropic triangle*

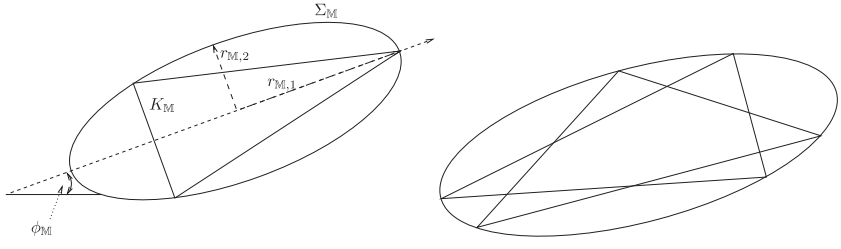

Fig. 1. The ellipse $\Sigma_{\mathbb{M}}$ with the length of semi-axes $r_{\mathbb{M},1}$, $r_{\mathbb{M},2}$ and the orientation $\phi_{\mathbb{M}}$, and the corresponding triangle $K_{\mathbb{M}}$ with the anisotropy $\{r_{\mathbb{M},1},\ r_{\mathbb{M},1}/r_{\mathbb{M},2},\ \phi_{\mathbb{M}}\}$ (left). The acute-angle and the obtuse-angle anisotropic triangles (right).

corresponding to $\mathbb{M}$. Hence, there is an isomorphism between the matrix $\mathbb{M}$, the corresponding ellipse $\Sigma_{\mathbb{M}}$ and the corresponding triangle $K_{\mathbb{M}}$.

Similarly as in [17,18,23,24] and the works cited therein, we describe the anisotropy of a triangle by three parameters: the *size*, the *aspect ratio* and the *orientation*.

Definition 2.1. Let $K_{\mathbb{M}}$ be the triangle corresponding to $\mathbb{M} \in Sym$ and $\lambda_{\mathbb{M},1}, \lambda_{\mathbb{M},2}$ and $\phi_{\mathbb{M}}$ be given by (1). Let $r_{\mathbb{M},i} = (\lambda_{\mathbb{M},i})^{-1/2}$, $i = 1,2$ be the lengths of semi-axes of $\Sigma_{\mathbb{M}}$. We say that

- $r_{\mathbb{M},1}$ is the *size* of $K_{\mathbb{M}}$,
- $\sigma_{\mathbb{M}} := \frac{r_{\mathbb{M},1}}{r_{\mathbb{M},2}} \geqslant 1$ is the *aspect ratio* of $K_{\mathbb{M}}$,
- $\phi_{\mathbb{M}}$ is the *orientation* of $K_{\mathbb{M}}$.

The triple $\{r_{\mathbb{M},1}, \sigma_{\mathbb{M}}, \phi_{\mathbb{M}}\}$ is called the *anisotropy* of $K_{\mathbb{M}}$.

Obviously, the matrix $\mathbb{M} \in Sym$ defines a Riemann metric in $\mathbb{R}^2$, where the distance of $x, y \in \mathbb{R}^2$ is given by $\|x-y\|_{\mathbb{M}} := \left((x-y)^{\mathrm{T}}\mathbb{M}(x-y)\right)^{1/2}$. For the purpose of the definition of an optimal *hp*-mesh, we recall one result from [9, Section 3].

Lemma 2.2. *Let $\mathbb{M} \in Sym$ and $K_{\mathbb{M}}$ be the corresponding triangle. Let $\boldsymbol{e}_i^{K_{\mathbb{M}}}$, $i = 1,2,3$ denote the edges of $K_{\mathbb{M}}$, which are considered as vectors from $\mathbb{R}^2$ given by their endpoints. Then*

$$\|\boldsymbol{e}_i^{K_{\mathbb{M}}}\|_{\mathbb{M}} := \left((\boldsymbol{e}_i^{K_{\mathbb{M}}})^{\mathrm{T}}\mathbb{M}\boldsymbol{e}_i^{K_{\mathbb{M}}}\right)^{1/2} = \sqrt{3}, \quad i = 1,2,3. \tag{3}$$

Hence, $K_{\mathbb{M}}$ is equilateral in the metric defined by $\mathbb{M}$.

Finally, let us note that it would be possible to consider also the obtuse-angle triangle, see Fig. 1, right. This triangle has the same area as the acute-angle one and its edges satisfy the assertion of Lemma 2.2, see [9, Section 3]. The in-house code ANGENER [25] used in this paper does not distinguish between the acute-angle and the obtuse-angle triangles, hence it generates also obtuse-angle triangles.

2.2. Anisotropic meshes

Similarly as in, e.g., [9–13,15], we define an anisotropic triangular grid $\mathcal{T}_h$ as a mesh consisting of equilateral triangles with respect to a given Riemann metric. Let $\mathcal{M} : \Omega \to Sym$ be an integrable mapping, which we call the *Riemann metric* on Ω. Let $\boldsymbol{v}_0, \boldsymbol{v}_1 \in \Omega$. We define the distance between $\boldsymbol{v}_0$ and $\boldsymbol{v}_1$ by

$$\|\boldsymbol{v}_1 - \boldsymbol{v}_0\|_{\mathcal{M}} := \int_0^1 \left((\boldsymbol{v}_1 - \boldsymbol{v}_0)^{\mathrm{T}}\mathcal{M}(\boldsymbol{v}_0 + t(\boldsymbol{v}_1 - \boldsymbol{v}_0))(\boldsymbol{v}_1 - \boldsymbol{v}_0)\right)^{1/2} \mathrm{d}t. \tag{4}$$

It is possible to prove that (4) defines a metric on Ω. In virtue of (3), it would be natural to define a mesh $\mathcal{T}_h$ such that

$$\|\boldsymbol{e}\|_{\mathcal{M}} = \sqrt{3} \quad \forall \boldsymbol{e} \in \mathcal{F}_h, \tag{5}$$

where $\mathcal{F}_h$ is the set of edges of $\mathcal{T}_h$. However, for the given metric $\mathcal{M}$, there does not exist (except special cases) any triangulation satisfying this requirement. Therefore, we define the triangulation *generated by metric* $\mathcal{M}$ such that the equalities (5) are satisfied approximately by the *least square technique*, see [9,10]. Hence:

Definition 2.3. Let $\mathcal{M}$ be the Riemann metric on Ω. We say that the triangulation $\mathcal{T}_h$ is *generated by metric* $\mathcal{M}$ if

$$\mathcal{T}_h = \arg\min_{\mathcal{T}_h} \sum_{\boldsymbol{e} \in \mathcal{F}_h'} \left(\|\boldsymbol{e}\|_{\mathcal{M}} - \sqrt{3}\right)^2, \tag{6}$$

where the minimum is taken over all possible triangulations $\mathcal{T}_h'$ of Ω and $\mathcal{F}_h'$ is the set of edges of $\mathcal{T}_h'$.

Let us note that there exist algorithms and codes, e.g., [25,26], which construct mesh $\mathcal{T}_h$ for the given metric $\mathcal{M}$ in the sense of Definition 2.3. Fig. 2 shows example of a metric $\mathcal{M}$ represented by the ellipses in selected nodes and the corresponding triangular grid.

2.3. Anisotropic hp-mesh

Let $\mathcal{T}_h = \{K\}$ be a triangulation of Ω. To each $K \in \mathcal{T}_h$, we assign a positive integer p_K (=local polynomial approximation degree on K). Then we define the *polynomial degree vector* $\mathsf{p} := \{p_K;\ K \in \mathcal{T}_h\}$. The pair $\mathcal{T}_{h\mathsf{p}} := \{\mathcal{T}_h, \mathsf{p}\}$ is called the *hp-mesh*.

In Section 2.2, we showed that the mapping $\mathcal{M} : \Omega \to Sym$ defines a triangular grid. On the other hand, the polynomial degree vector $\mathsf{p} = \{p_K;\ K \in \mathcal{T}_h\}$ can be defined in the following way.

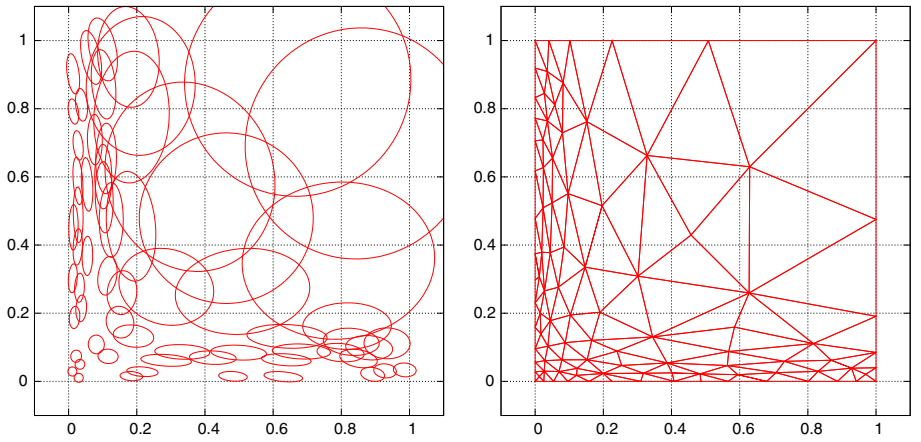

Fig. 2. Example of an metric $\mathcal{M}$ represented by ellipses in selected nodes (left) and the corresponding triangular grid (right).

Definition 2.4. Let $\mathcal{P}:\Omega\to\mathbb{R}^+$ be a given integrable function, which we call the *polynomial degree distribution function*. Let $\mathcal{T}_h$ be a triangulation of Ω, using $\mathcal{P}$, we define the polynomial degree vector $\mathsf{p}=\{p_K;\ K\in\mathcal{T}_h\}$ by

$$p_K := \mathrm{int}\left[\frac{1}{|K|}\int_K \mathcal{P}(x)\mathrm{d}x\right],\quad K\in\mathcal{T}_h, \tag{7}$$

where $\mathrm{int}[a]:=\lfloor a+1/2\rfloor$ denotes the integer part of the number $a+1/2,\ a\geqslant 0$.

Therefore, for the given Riemann metric $\mathcal{M}:\Omega\to Sym$ and for the given polynomial degree distribution function $\mathcal{P}:\Omega\to\mathbb{R}^+$, we are able to construct the *hp*-mesh $\mathcal{T}_{h\mathsf{p}}=\{\mathcal{T}_h,\mathsf{p}\}$ where $\mathcal{T}_h$ and p are given by Definitions 2.3 and 2.4, respectively. Let us note that in practice, it is sufficient to evaluate $\mathcal{M}$ and $\mathcal{P}$ only in a finite number of nodes $x\in\Omega$.

3. Optimal anisotropic *hp*-mesh for a given function $u:\Omega\to\mathbb{R}$

This section exhibits a theoretical background of the presented *hp*-adaptation algorithm, which was developed in [21]. We recall the construction of the optimal anisotropic *hp*-mesh for the given function $u:\Omega\to\mathbb{R}$. The optimality is based on the minimization of number of degrees of freedom provided that the interpolation error is under a given tolerance. For simplicity, we deal with functions from $V:=C^\infty(\Omega)$.

3.1. The main problem

For the given *hp*-mesh $\mathcal{T}_{h\mathsf{p}}=\{\mathcal{T}_h,\mathsf{p}\}$, we define the space of discontinuous piecewise polynomial functions by

$$S_{h\mathsf{p}} := \{v\in L^2(\Omega);\ v|_K\in P^{p_K}(K)\ \forall K\in\mathcal{T}_h\}, \tag{8}$$

where $P^{p_K}(K)$ is the space of polynomials of degree $\leqslant p_K$ on $K\in\mathcal{T}_h$. The dimension of $S_{h\mathsf{p}}$ is equal to $N_{h\mathsf{p}}:=\sum_{K\in\mathcal{T}_h}(p_K+1)(p_K+2)/2$, which is called the *number of degrees of freedom* of the *hp*-mesh $\mathcal{T}_{h\mathsf{p}}$.

Let $u\in V$ be a given function, $\bar{x}\in\Omega$ and $p\in\mathbb{N}$ be an integer. We define the projection operator $\pi_{\bar{x},p}:V\to P^p(\bar{\Omega})$ such that

$$\frac{\partial^k \pi_{\bar{x},p}u(\bar{x})}{\partial x_1^l\partial x_2^{k-l}} = \frac{\partial^k u(\bar{x})}{\partial x_1^l\partial x_2^{k-l}}\quad \forall l=0,\dots,k\quad \forall k=0,\dots,p. \tag{9}$$

Therefore, $\pi_{\bar{x},p}u$ is the polynomial function of degree p on Ω which has the same values of all partial derivatives up to order p at $\bar{x}$ as the function u. The existence and uniqueness of $\pi_{\bar{x},p}u$ is obvious. Using the operator $\pi_{\bar{x},p}$, we define the projection into the space $S_{h\mathsf{p}}$.

Definition 3.1. Let $\mathcal{T}_{h\mathsf{p}}=(\mathcal{T}_h,\mathsf{p})$ be a *hp*-mesh, $x_K,\ K\in\mathcal{T}_h$ be the barycentres of $K\in\mathcal{T}_h$ and $S_{h\mathsf{p}}$ be the corresponding space of discontinuous piecewise polynomial functions given by (8). We define the operator $\Pi_{h\mathsf{p}}:V\to S_{h\mathsf{p}}$ by

$$\Pi_{h\mathsf{p}}u|_K := \pi_{x_K,p_K}u|_K\quad \forall K\in\mathcal{T}_h, \tag{10}$$

where π_{x_K,p_K} is given by (9). The operator $\Pi_{h\mathsf{p}}$ is defined separately for each $K\in\mathcal{T}_h$ and it is unique for the given *hp*-mesh.

Now, we are ready to formulate the following problem.

Problem 3.2. Let $u\in V$ be a given function, $q\in[1,\infty]$ be a given degree of the Lebesgue norm and $\omega>0$ be a given tolerance. We *seek a hp-mesh* $\mathcal{T}_{h\mathsf{p}}$ such that

(P1) $\|u - \Pi_{hp} u\|_{L^q(\Omega)} \leqslant \omega$, where $\Pi_{hp} : V \to S_{hp}$ is defined by (10),
(P2) the number of degrees of freedom N_{hp} of $\mathcal{T}_{hp}$ is minimal.

The Problem 3.2 is complex and we are not able to solve it. Therefore, in [21] we developed an algorithm, which generates an anisotropic *hp*-grid such that condition (P1) of Problem 3.2 is satisfied up to the higher order terms and the corresponding number N_{hp} is small. Therefore, we expect that this resulting *hp*-mesh is close to the (hypothetical) solution of Problem 3.2. The algorithm from [21] consists of the following steps:

1. Let $\bar{x} \in \Omega$ be given.
2. For any polynomial degree $p = 1, 2, \ldots$, we consider an *auxiliary* local *problem* whose solution results the **ratio** and the **orientation** of the anisotropic triangle with the barycentre at $\bar{x}$.
3. With the aid condition (P1) of Problem 3.2, we fix the **size** of this triangle with the barycentre at $\bar{x}$.
4. Among all degrees $p = 1, 2, \ldots$, we choose the optimal **polynomial approximation degree** (and the corresponding triangle represented by a matrix from *Sym*), which gives the least number of degrees of freedom per unit area (for the given tolerance ω).

Performing these steps (theoretically) for all $\bar{x} \in \Omega$, we derive the Riemann metric $\mathcal{M} : \Omega \to Sym$ and the polynomial degree distribution function $\mathcal{P} : \Omega \to \mathbb{R}^+$, which define the *hp*-mesh $\mathcal{T}_{hp}$. Let us recall that in practice, it is sufficient to evaluate $\mathcal{M}$ and $\mathcal{P}$ only in a finite number of nodes $\bar{x} \in \Omega$.

In the rest of this section, we briefly describe these steps, all details can be found in [21].

3.2. Setting of the ratio and the orientation of a triangle for the given p

Let $u \in V,\ \bar{x} = (\bar{x}_1, \bar{x}_2) \in \Omega$ and $p \in \mathbb{N}$ be given. Let $\pi_{\bar{x},p} u$ be given by (9), then using the Taylor expansion of degree $p+1$ at $\bar{x}$, we have

$$u(x) - \pi_{\bar{x},p} u(x) = e^{\mathrm{int}}_{\bar{x},p}(x) + O(|x - \bar{x}|^{p+2}), \tag{11}$$

where

$$e^{\mathrm{int}}_{\bar{x},p}(x) := \frac{1}{(p+1)!} \sum_{l=0}^{p+1} \binom{p+1}{l} \frac{\partial^{p+1} u(\bar{x})}{\partial x_1^l \partial x_2^{p+1-l}} (x_1 - \bar{x}_1)^l (x_2 - \bar{x}_2)^{p+1-l} \tag{12}$$

is the *interpolation error function* of degree p located at $\bar{x}$. Let us note that the right-hand side of (12) is the $(p+1)^{\mathrm{th}}$-order scaled directional derivative of u at $\bar{x}$ along the direction $x - \bar{x}$. Obviously, $e^{\mathrm{int}}_{\bar{x},p}(\bar{x}) = 0$ and $e^{\mathrm{int}}_{\bar{x},p}(x) \approx u(x) - \pi_{\bar{x},p} u(x)$ up to the higher order terms. Finally, (10) and (11) give

$$(u - \Pi_{hp} u)|_K \approx e^{\mathrm{int}}_{x_K, p_K}|_K \quad \forall K \in \mathcal{T}_h, \tag{13}$$

where x_K is the barycentre of $K \in \mathcal{T}_h$.

Based on (13), we introduce the following *auxiliary local problem*.

Problem 3.3. Let $u \in V,\ \bar{x} \in \Omega,\ p \in \mathbb{N},\ q \in [1, \infty]$ and $\bar{\omega} > 0$ be given. We seek an *anisotropic triangle* K (i.e., its anisotropy $\{h_K, \sigma_K, \phi_K\}$) having the barycentre at $\bar{x}$ such that

(p1) $\left\| e^{\mathrm{int}}_{\bar{x},p} \right\|_{L^q(K)} \leqslant \bar{\omega}$,
(p2) the area of K is the maximal possible.

The condition (p2) follows from the consideration that in order to minimize the number N_{hp} of the *hp*-mesh, we have to construct triangles with the maximal possible area (for the given polynomial approximation degree). The tolerance $\bar{\omega}$ will be specified later.

We simply observe that the interpolation error function $e^{\mathrm{int}}_{\bar{x},p}$ depends in general on all partial derivatives of order $p+1$ of u. On the other hand, the anisotropy of a triangle is given by three parameters. Therefore, in order to solve Problem 3.3, it is advantageous to estimate $e^{\mathrm{int}}_{\bar{x},p}$ by an expression depending on three parameters only. Motivated by Cao [17,18], we derived in [21] the following *estimate of the interpolation error functions*

$$\left| e^{\mathrm{int}}_{\bar{x},p}(x) \right| \leqslant A_p \left((x - \bar{x})^{\mathrm{T}} \mathbb{Q}_{\varphi_p} \mathbb{D}_{\rho_p} \mathbb{Q}^{\mathrm{T}}_{\varphi_p} (x - \bar{x}) \right)^{\frac{p+1}{2}} \ \forall\, x \in \Omega, \tag{14}$$

where $A_p > 0,\ \mathbb{Q}_{\varphi_p}$ is the rotation through angle φ_p and $\mathbb{D}_{\rho_p}$ is the matrix given by

$$\mathbb{D}_\rho := \begin{pmatrix} 1 & 0 \\ 0 & \rho^{-\frac{2}{p+1}} \end{pmatrix}, \quad \rho \geqslant 1. \tag{15}$$

The values $A_p \geqslant 0,\ \rho_p \geqslant 1$ and $\varphi_p \in [0, 2\pi)$ represent the *size*, the *aspect ratio* and the *orientation* of the interpolation error function $e^{\text{int}}_{\bar{x},p}$, which are defined in such a way that the estimate (14) is as sharp as possible in the following sense:

Obviously, both sides of (14) are $(p+1)$-homogeneous functions of $(x-\bar{x})$, i.e., $f(x-\bar{x}) = |x-\bar{x}|^{p+1} f\left(\frac{x-\bar{x}}{|x-\bar{x}|}\right)$. Moreover, both sides of (14) define bounded domains F^p and G^p in $\mathbb{R}^2$, namely F^p and G^p are the interiors of the closed curves

$$\left\{y \in \mathbb{R}^2;\ y = \left|e^{\text{int}}_{\bar{x},p}(x)\right|(x-\bar{x}),\ |x-\bar{x}| = 1\right\} \text{ and } \left\{y \in \mathbb{R}^2;\ y = A_p\left((x-\bar{x})^{\mathrm{T}} \mathbb{Q}_{\varphi_p} \mathbb{D}_{\rho_p} \mathbb{Q}^{\mathrm{T}}_{\varphi_p}(x-\bar{x})\right)^{\frac{p+1}{2}}(x-\bar{x}),\ |x-\bar{x}| = 1\right\}, \tag{16}$$

respectively.

Obviously, if $F^p \subset G^p$ then estimate (14) is valid. Therefore, in order to guarantee a sharpness of (14), we set parameters $A_p \geqslant 0,\ \rho_p \geqslant 1$ and $\varphi_p \in [0, 2\pi)$ in such a way that $F^p \subset G^p$ and the area of G^p is minimal. This triplet $\{A_p,\ \rho_p,\ \varphi_p\}$ is called the *anisotropy* of the interpolation error function $e^{\text{int}}_{\bar{x},p}$.

Let $\{\tilde{A}_p,\ \tilde{\rho}_p,\ \tilde{\varphi}_p\}$ be a triplet, where $\tilde{A}_p$ is the maximal value of the $(p+1)^{\text{th}}$-order scaled directional derivative of u at $\bar{x}$, $\tilde{\varphi}_p$ is the angle of the direction of the maximal derivative and $\tilde{\rho}_p$ is the ratio between $\tilde{A}_p$ and the $(p+1)^{\text{th}}$-order scaled directional derivative along the perpendicular direction. Let g^p be the set defined as G^p in (16) but with $\{\tilde{A}_p,\ \tilde{\rho}_p,\ \tilde{\varphi}_p\}$. In certain cases, $F^p \subset g^p$ then we put $\{A_p,\ \rho_p,\ \varphi_p\} := \{\tilde{A}_p,\ \tilde{\rho}_p,\ \tilde{\varphi}_p\}$.

However, in a general case, $F^p \not\subset g^p$ (see Fig. 3 introduced bellow), hence (14) is not valid for $\{A_p,\ \rho_p,\ \varphi_p\} := \{\tilde{A}_p,\ \tilde{\rho}_p,\ \tilde{\varphi}_p\}$. Therefore, the triplet $\{\tilde{A}_p,\ \tilde{\rho}_p,\ \tilde{\varphi}_p\}$ has to be modified in such a way that the corresponding set G^p is increased in order to contain F^p. For the detailed determination of $\{A_p,\ \rho_p,\ \varphi_p\}$, see [21, Section 3.2].

Fig. 3 shows the sets $F^p,\ g^p$ and G^p for $p = 1, 3, 5,\ \bar{x} = (1, 1)$ and u given by

$$u(x_1, x_2) = 0.01\left(6x_1^7 + 4x_1^6x_2 - 3x_1^5x_2^2 + 8x_1^4x_2^3 + 12x_1^3x_2^4 + 5x_1^2x_2^5 + x_1x_2^6 - x_2^7\right). \tag{17}$$

The estimate (14) is the base for the solution of Problem 3.3 formulated in the following Lemma, for the proof see [21, Lemma 3.17].

Lemma 3.4. *Let $u \in V,\ \bar{x} \in \Omega,\ p \in \mathbb{N},\ q \in [1, \infty]$ and $\bar{\omega} > 0$ be given. Let $\{A_p,\ \varphi_p,\ \rho_p\}$ be the anisotropy of the corresponding interpolation error function $e^{\text{int}}_{\bar{x},p}$. We set $v_{\bar{x},p}$ by*

$$v_{\bar{x},p} := \left(\bar{\omega}\rho_p^{\frac{1}{2}}/(c_{p,q}A_p)\right)^{\frac{2q}{q(p+1)+2}} \text{ for } q \in [1, \infty), \quad v_{\bar{x},p} := \left(\bar{\omega}\rho_p^{\frac{1}{2}}/A_p\right)^{\frac{2}{p+1}} \text{ for } q = \infty, \tag{18}$$

where $c_{p,q} := \left(\frac{2(\pi)^{\frac{-q(p+1)}{2}}}{q(p+1)+2}\right)^{1/q}$ and $\pi = 3.1415\ldots$. Then the triangle $K_{\bar{x},p}$ with the anisotropy $\{h_E, \sigma_E, \phi_E\}$ given by

$$h_E = \left(\rho_p^{\frac{1}{p+1}} v_{\bar{x},p}/\pi\right)^{1/2}, \quad \sigma_E = \rho_p^{\frac{1}{p+1}}, \quad \phi_E = \varphi_p - \pi/2 \tag{19}$$

is (almost) the solution of Problem 3.3, namely we have

$$\left\|e^{\text{int}}_{\bar{x},p}\right\| L^q(K_{\bar{x},p}) \leqslant c_{p,q}A_p\rho_p^{-\frac{1}{2}}\left(v_{\bar{x},p}\right)^{\frac{q(p+1)+2}{2q}} = \bar{\omega}, \quad q < \infty \qquad \text{and} \qquad \left\|e^{\text{int}}_{\bar{x},p}\right\| L^\infty(K_{\bar{x},p}) \leqslant A_p\rho_p^{-\frac{1}{2}}\left(v_{\bar{x},p}\right)^{\frac{p+1}{2}} = \bar{\omega}. \tag{20}$$

Finally, let us note $v_{\bar{x},p}$ is equal to the area of element (up to a multiplicative constant) and due to (18), it is related to the local tolerance $\bar{\omega}$. It will be specified in the following section.

3.3. Setting of the size of a triangle

Here, we present only the more complicated case $q < \infty$. We need to set the area $v_{\bar{x},p}$ of a triangle, i.e., its size since its ratio was already specified. The main Problem 3.2 requires the error bound $\|u - \Pi_{h_\mathcal{D}} u\|_{L^q(\Omega)} \leqslant \omega$, where $\omega > 0$ is the given (global) tolerance. In order to set $\bar{\omega}$ in Problem 3.3, we use the implication

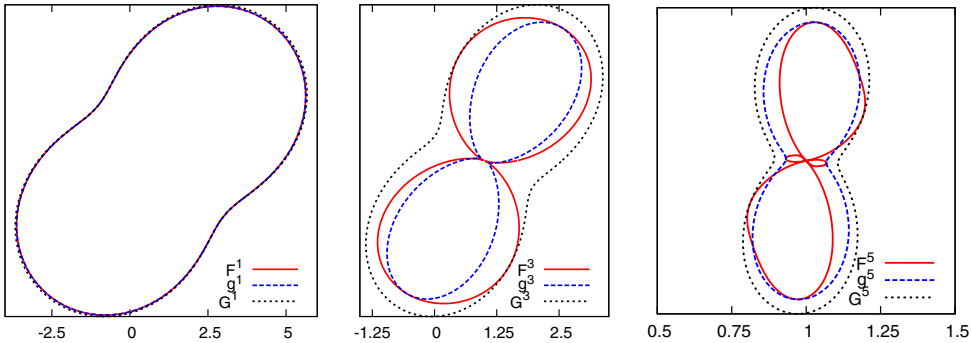

Fig. 3. The boundaries of domains F^p, g^p and G^p for function (17).

$$\|u-\Pi_{hp}u\|_{L^q(\Omega)} \leqslant \omega \qquad \Leftarrow \qquad \|u-\Pi_{hp}u\|_{L^q(K)} \leqslant \omega(|K|/|\Omega|)^{1/q} \quad \forall K\in\mathcal{T}_h. \tag{21}$$

Although the *equidistribution condition* on the right-hand side of (21) *does not guarantee* that the resulting grid is the globally optimal grid, we employ it for the setting of the local tolerance $\bar{\omega}$ in (18), since we do know how to solve this complex problem in an effective way.

In virtue of (13) and the right-hand side of (21), we require that

$$\left\|e^{\mathrm{int}}_{\bar{x},p}\right\|_{L^q(K_{\bar{x},p})} \leqslant \omega\big(v_{\bar{x},p}/|\Omega|\big)^{\frac{1}{q}}. \tag{22}$$

Hence, in order to specify area $v_{\bar{x},p}$, using (20) and (22), we set the condition $c_{p,q}A_p\rho_p^{-\frac{1}{2}}\big(v_{\bar{x},p}\big)^{\frac{q(p+1)+2}{2q}} = \omega\big(v_{\bar{x},p}/|\Omega|\big)^{\frac{1}{q}}$, which implies

$$v_{\bar{x},p} = |\Omega|^{-\frac{2}{q(p+1)}}\Big(\omega\rho_p^{\frac{1}{2}}/(c_{p,q}A_p)\Big)^{\frac{2}{p+1}}. \tag{23}$$

3.4. Choice of the polynomial approximation degree

In previous sections, we have derived the anisotropy of the optimal triangle $K_{\bar{x},p}$, which minimizes the norm of the interpolation error function $e^{\mathrm{int}}_{\bar{x},p}$ on $K_{\bar{x},p}$ for any $\bar{x}\in\Omega$ and for the arbitrary given polynomial approximation degree p. In this section, we set the optimal polynomial degree p.

We introduced the so-called *density of the number of degrees of freedom* by

$$\eta_p(\bar{x}) := \frac{(p+1)(p+2)}{2v_{\bar{x},p}}, \quad p\in\mathbb{N},\ \bar{x}\in\Omega \tag{24}$$

representing the number of degree of freedom per unit area. Then, for each $\bar{x}\in\Omega$, we choose the polynomial degree $p\in\mathbb{N}$ such that the corresponding value $\eta_{\bar{x},p}$ is minimal, i.e., we put

$$p_{\bar{x}} := \arg\min_{p\in\mathbb{N}}\eta_p(\bar{x}). \tag{25}$$

Let us note that in practical implementation, the degree p is bounded from above by the maximal implemented polynomial approximation degree, hence the minimum in (25) always exists.

3.5. Anisotropic hp-adaptation algorithm

Now we are ready to define the Riemann metric $\mathcal{M}$ and the polynomial degree distribution function $\mathcal{P}$, which generate the *hp*-mesh $\mathcal{T}_{hp}$ by Definitions 2.3 and 2.4, such that $\mathcal{T}_{hp}$ is close to the solution of the main Problem 3.2. We define the following algorithm.

Algorithm (A) (*Generation* of $\mathcal{M}(x)$ and $\mathcal{P}(x)$ for $x\in\Omega$). Let $u\in V,\ q\in[1,\infty]$ and $\omega>0$ be given. Then

1. For each $p=1,2,\ldots,$
   (a) We evaluate the anisotropy of the interpolation error function $\{A_p,\varphi_p,\rho_p\}$ introduced in Section 3.2.
   (b) Using (23), we set the area $v_p(x)$ of the triangle $K_{x,p}$.
   (c) Using relation (19), we define the optimal anisotropy of $K_{x,p}$ by the triple $\{h_E(x),\ \sigma_E(x),\ \phi_E(x)\}$.
   (d) Using Definition 2.1, we find matrix $\mathbb{M}_p(x)$ defining triangle with the anisotropy $\{h_E(x),\sigma_E(x),\phi_E(x)\}$.
   (e) Using (24), we evaluate the quantity $\eta_p(x) := (p+1)(p+2)/(2v_p(x))$.
2. We find $p_x\in\mathbb{N}$ minimizing $\eta_p(x)$, i.e. $p_x := \arg\min_{p\in\mathbb{N}}\eta_p(x)$.
3. We set $\mathcal{M}(x) := \mathbb{M}_{p_x}(x)$ and $\mathcal{P}(x) := p_x$.

Theoretically, we can employ the previous algorithm for any $x\in\Omega$. In practical application, we evaluate $\mathcal{M}$ and $\mathcal{P}$ only for the finite number of $x\in\Omega$ and then we continuously interpolate $\mathcal{M}$ and $\mathcal{P}$ on Ω.

4. Application of the anisotropic *hp*-adaptation to steady problems

In Section 3, we presented the algorithm, which generates, for a given function u, the anisotropic *hp*-grid such that the interpolation error is under the given tolerance and the number of degrees of freedom N_{hp} is small. We apply this algorithm for the numerical solution of a boundary value problem (BVP).

4.1. Definition of the adaptation process

Let $u:\Omega\to\mathbb{R}$ be the exact solution of the given BVP. The goal is to find a *hp*-mesh (and the corresponding space S_{hp} given by (8)) such that the approximate solution $u_{hp}\in S_{hp}$ satisfies

$$\left\|\tilde{u}_{h\mathrm{p}} - \Pi_{h\mathrm{p}}\tilde{u}_{h\mathrm{p}}\right\|_{L^q(\Omega)} \leqslant \omega, \tag{26}$$

where $\tilde{u}_{h\mathrm{p}}$ is a higher order reconstruction of the approximate solution $u_{h\mathrm{p}}$, namely $\tilde{u}_{h\mathrm{p}}|_K \in P^{p_K+1}(K),\ K \in \mathcal{T}_h$ (see Section 4.2 for the definition of this reconstruction). The final (optimal) *hp*-grid is obtained iteratively after several adaptations with the aid of Algorithm (A) from Section 3.5. Particularly, if $u_{h\mathrm{p}}$ is an approximate solution of BVP obtained on the given *hp*-mesh $\mathcal{T}_{h\mathrm{p}}$ then we generate a new (better) mesh $\mathcal{T}_{h\mathrm{p}}^N$ where the more accurate approximate solution can be obtained. In the following we describe the implementation of Algorithm (A) with the aid of the software package ANGENER [25]. If a triangular grid $\mathcal{T}_h$ is given together with the metric $\mathcal{M}$ evaluated at the barycentres x_K of all $K \in \mathcal{T}_h$, then ANGENER creates a new anisotropic triangular grid in the sense of Definition 2.3. Therefore, for our purposes, it is sufficient to perform Algorithm (A) only for $x_K,\ K \in \mathcal{T}_h$.

4.2. Implementation of Algorithm (A)

Since the optimal mesh is sought iteratively, it makes no sense to test all possible polynomial approximation degrees in the step (1) of Algorithm (A). Therefore, if K is an element from the initial mesh $\mathcal{T}_{h\mathrm{p}}$ and p_K the corresponding polynomial approximation degree then we perform the step (1) of Algorithm (A) only for $p := p_K - 1,\ p := p_K$ and $p := p_K + 1$.

Moreover, in the step (a) of Algorithm (A), we approximate the $p+1$ directional derivative of $u_{h\mathrm{p}}$ for $p = p_K - 1,\ p_K,\ p_K + 1$ in the following way. For each $K \in \mathcal{T}_h$, we define the patch $D(K)$ which consists of all $K' \in \mathcal{T}_h$ sharing a face with K. Then we define the polynomial function $\tilde{u}_{K,p} \in P^{p+1}(D(K))$ by

$$\left(\tilde{u}_{K,p}, \phi\right)_{1,D(K)} = \left(u_{h\mathrm{p}}, \phi\right)_{1,D(K)} \quad \forall \phi \in P^{p+1}(D(K)), \tag{27}$$

where $P^{p+1}(D(K))$ is the space of polynomial functions of degree $p+1$ on $D(K)$ and $(\cdot,\cdot)_{1,D(K)}$ is the H^1-scalar product on $D(K)$. Then the partial derivative of degree $p+1$ of $\tilde{u}_{K,p}$ are constant on K and in step (a) of Algorithm (A), where we evaluate $A_p,\ \varphi_p$ and ρ_p, we replace u by $\tilde{u}_{K,p}$.

Hence, the output of the implemented algorithm are $\mathcal{M}(x_K) \in Sym,\ \mathcal{P}(x_K) \in \mathbb{N}\ \forall K \in \mathcal{T}_h$. The matrices $\mathcal{M}(x_K),\ K \in \mathcal{T}_h$ are passed to ANGENER which generates a new mesh $\mathcal{T}_h^N$. Finally, for each vertex x_P of the old mesh $\mathcal{T}_h$, we set $\mathcal{P}(x_P) \in \mathbb{R}^+$ as the average of $\mathcal{P}(x_K)$ for all K having x_P as a vertex. Then, we obtain a continuous piecewise linear function $\mathcal{P} : \Omega \to \mathbb{R}^+$ on $\mathcal{T}_h$ and using (7) we compute the polynomial approximation degrees on the new mesh $\mathcal{T}_h^N$.

Remark 4.1. Let us note that it is difficult to achieve the condition (26) in a reasonable small number of adaptation levels by applying Algorithm (A) since the algorithm tries to achieve relation (26) with the equality. Moreover, not all operations in ANGENER are allowed in order to ensure, e.g., the shape-regularity of the meshes. Therefore, in practice, for given ω we employ Algorithm (A) with $\omega := z\omega$ where $z = 0.1$ or $z = 0.2$.

5. Application of the anisotropic *hp*-adaptation to time-dependent problems

In previous sections, we described the construction of an anisotropic *hp*-mesh for the numerical solution of steady (boundary values) problems. In this section, we extend this approach to the numerical solution of time-dependent problems given generally by

$$\frac{\partial u}{\partial t} + \mathcal{A}u = 0 \quad \text{in} \quad Q_T := \Omega \times (0,T), \tag{28}$$

where $u : \Omega \times (0,T) \to \mathbb{R}$ is the sought solution, $\Omega \subset \mathbb{R}^2$ is the computational domain, $T > 0$ is the final time and $\mathcal{A}$ is a (non-linear) differential operator. This equation has to be accompanied by suitable initial and boundary conditions.

5.1. Space–time discretization

It is advantageous to discretize problem (28) by a method, which simply employ different meshes on different time levels. Therefore, we employ the *space–time discontinuous Galerkin* (STDG) method, e.g., [27–31].

Let $0 = t_0 < \cdots < t_r = T$ be a partition of $(0,T),\ r > 0$ is integer and $I_m = (t_{m-1}, t_m),\ m = 1,\ldots,r$. By $\{v\}_m$ we denote the jump of $v : \bigcup_{m=1}^r I_m \to \mathbb{R}$ at t_m given by

$$\{v\}_m = v_m^+ - v_m^-, \quad v_m^\pm = v(t_m\pm) = \lim_{t\to t_m\pm} v(t) \tag{29}$$

provided the one-sided limits $\lim_{t\to t_m\pm} v(t)$ exist.

For each time instant $t_m,\ m = 0,\ldots,r$, and interval $I_m,\ m = 1,\ldots,r$, we consider a conforming *hp*-mesh $\mathcal{T}_{h\mathrm{p}}^{(m)}$. Let $S_{h\mathrm{p}}^{(m)}$ be the space of (space) piecewise polynomial functions on $\mathcal{T}_{h\mathrm{p}}^{(m)},\ m = 0,\ldots,r$ given by (8), we define the space of discontinuous piecewise-polynomial function on $\{\mathcal{T}_{h\mathrm{p}}^{(m)},\ m = 1,\ldots,r\}$ by

$$S_{h\mathrm{p}}^{\tau k} := \left\{ v \in L^2(Q_T);\ v(x,t)\Big|_{I_m} = \sum_{i=0}^{k} t^i\, v_{m,i}(x) \text{ with } v_{m,i} \in S_{h\mathrm{p}}^{(m)},\ i = 0,\ldots,k,\ \ m = 1,\ldots,r \right\}, \tag{30}$$

where the integer $k \geqslant 0$ denotes the polynomial approximation degree with respect to the time coordinate.

Then, the STDG discretization of (28) reads: wee seek $u_h \in S_{h\mathrm{p}}^{\tau k}$ such that

$$\int_{I_m} \left(\left(\frac{\partial u_h}{\partial t}, v_h \right) + a_h^{(m)}(u_h, v_h) \right) \mathrm{d}t + \left(\{u_h\}_{m-1}, (v_h)_{m-1}^+ \right) = 0 \quad \forall v_h \in S_{h\mathrm{p}}^{\tau k},\ m = 1, \ldots, r, \tag{31}$$

where $(\cdot,\cdot)$ denotes the L^2-scalar product over Ω and $a_h^{(m)} : S_{h\mathrm{p}}^{(m)} \times S_{h\mathrm{p}}^{(m)} \to \mathbb{R}$ represents the (space) discontinuous Galerkin discretization of the differential operator $\mathcal{A}$. The function $(u_h)_0^-$ is given by the initial condition. For more details see, e.g., [32,33].

The coupling between two time levels is performed by the second term in (31)

$$\left(\{u_h\}_{m-1}, (v_h)_{m-1}^+ \right) = \left((u_h)_{m-1}^+, (v_h)_{m-1}^+ \right) - \left((u_h)_{m-1}^-, (v_h)_{m-1}^+ \right), \quad (u_h)_{m-1}^+, (v_h)_{m-1}^+ \in S_{h\mathrm{p}}^{(m)}, \quad (u_h)_{m-1}^- \in S_{h\mathrm{p}}^{(m-1)},$$

where the last term is the integral of the product of a function from $\mathcal{T}_{h\mathrm{p}}^{(m-1)}$ with a function from $\mathcal{T}_{h\mathrm{p}}^{(m)}$. Obviously,

$$\left((u_h)_{m-1}^-, (v_h)_{m-1}^+ \right) = \left(P_{h\mathrm{p}}^{(m)} (u_h)_{m-1}^-, (v_h)_{m-1}^+ \right), \quad (v_h)_{m-1}^+ \in S_{h\mathrm{p}}^{(m)},$$

where $P_{h\mathrm{p}}^{(m)} (u_h)_{m-1}^- \in S_{h\mathrm{p}}^{(m)}$ is the L^2-projection of $(u_h)_{m-1}^- \in S_{h\mathrm{p}}^{(m-1)}$ on the mesh $\mathcal{T}_{h\mathrm{p}}^{(m)}$. Therefore, (31) can be replaced by

$$\int_{I_m} \left(\left(\frac{\partial u_h}{\partial t}, v_h \right) + a_h^{(m)}(u_h, v_h) \right) \mathrm{d}t + \left((u_h)_{m-1}^+ - P_{h\mathrm{p}}^{(m)} (u_h)_{m-1}^-, (v_h)_{m-1}^+ \right) = 0 \quad \forall v_h \in S_{h\mathrm{p}}^{\tau k},\ m = 1, \ldots, r. \tag{32}$$

5.2. Implementation comments

The STDG formulation (31) represents a system on nonlinear algebraic equations, which are solved by a Newton-like method. The Jacobian matrix is replaced by the so-called flux matrix (see [34]) which can be derived analytically. The Newton-like iterative process is performed until the algebraic error does not significantly influence the space discretization error. Moreover, the time step is chosen adaptively is such a way that the discretization error arising from the time discretization does not significantly influence the space discretization error. A detailed description of these error estimates for the STDG method is the subject of the forthcoming paper [35].

Let us note that the discontinuous Galerkin discretization with respect to the time is rather expensive since the size of the corresponding nonlinear algebraic system is proportional to $k+1$ (in contrary to, e.g., the Runge–Kutta methods, the BDF schemes). On the other hand, it is very accurate therefore significantly smaller number of time steps is sufficient, see Table 2 bellow.

5.3. Mesh adaptation

An efficient numerical solution of time-dependent problems requires several re-meshing of grids during the computational process. However, each re-meshing requires some additional computational time. Taking into account the mesh adaptation method introduced in the previous sections, we develop the anisotropic *hp*-adaptation technique, which control the interpolation error in the "discrete $L^\infty(0,T;L^q(\Omega))$-norm", namely

$$\left\| E_{\mathrm{I}}^{(m)} \right\|_{L^q(\Omega)} \leqslant \omega \quad \forall m = 0, \ldots, r, \quad \text{with} \quad E_{\mathrm{I}}^{(m)} := u_m^- - \Pi_{h\mathrm{p}}^{(m)} u_m^-, \tag{33}$$

where $u : \Omega \times (0,T) \to \mathbb{R}$ be the exact solution of (28) and $\Pi_{h\mathrm{p}}^{(m)}$ is the projection into $S_{h\mathrm{p}}^{(m)}$ defined by (10).

Thus, in virtue of Problem 3.2, we formulate the following problem.

Problem 5.1. Let $u : \Omega \times (0,T) \to \mathbb{R}$ be a given function, $q \in [1,\infty]$ be a given degree of the Lebesgue norm and $\omega > 0$ be a given tolerance. We *seek a sequence of hp-grids* $\mathcal{T}_{h\mathrm{p}}^{(m)},\ m = 0, \ldots, r$ such that

($P1^\star$)

$$\left\| u_m^- - \Pi_{h\mathrm{p}}^{(m)} u_m^- \right\|_{L^q(\Omega)} \leqslant \omega, \quad m = 0, \ldots, r, \tag{34}$$

where $\Pi_{h\mathrm{p}}^{(m)}$ is the projection into $S_{h\mathrm{p}}^{(m)}$ defined by (10),

($P2^\star$) the number of degrees of freedom $N_{h\mathrm{p}}^{(m)}$ of $\mathcal{T}_{h\mathrm{p}}^{(m)},\ m = 0, \ldots, r$ is as small as possible.

The resulting algorithm for the solution of problem (28) is based on the following steps:

(S1) let the inequality from condition ($P1^\star$) be satisfied for some $m-1$ for a *hp*-mesh $\mathcal{T}_{h\mathrm{p}}^{(m-1)}$,
(S2) we put $\mathcal{T}_{h\mathrm{p}}^{(m)} := \mathcal{T}_{h\mathrm{p}}^{(m-1)}$ and perform the computation between time levels t_{m-1} and t_m on $\mathcal{T}_{h\mathrm{p}}^{(m)}$,
(S3) if ($P1^\star$) is valid for m then we put $m := m+1$ proceed to the new step,
(S4) otherwise, we construct new (better) *hp*-mesh $\mathcal{T}_{h\mathrm{p}}^{(m)}$ and repeat the computation from t_{m-1} to t_m.

The most important aspect is the construction of the *hp*-mesh $\mathcal{T}_{hp}^{(m)}$ in step (S4) since we need to approximate the solution between time levels t_{m-1} and t_m sufficiently accurately. Therefore, in virtue of (32), we construct $\mathcal{T}_{hp}^{(m)}$ using the functions $P_{hp}^{(m)}(\tilde{u}_h)_{m-1}^-$ and $(\tilde{u}_h)_m^-$, where $\tilde{u}_h$ is a higher order reconstruction of u_h, cf. (26). We employ the technique of an *intersection of metrics* developed in [36]. At each node of consideration, we construct two ellipses representing the metric generated by both functions. Then the resulting metric corresponds to an ellipse having the maximal possible area and which is contained in the intersection of both original ellipses, see Fig. 4. This construction implies that the conditions

$$\left\| P_{hp}^{(m)}(\tilde{u}_h)_{m-1}^- - \Pi_{hp}^{(m)}(P_{hp}^{(m)}(\tilde{u}_h)_{m-1}^-) \right\|_{L^q(\Omega)} \leqslant \omega \quad \text{and} \quad \left\| (\tilde{u}_h)_m^- - \Pi_{hp}^{(m)}(\tilde{u}_h)_m^- \right\|_{L^q(\Omega)} \leqslant \omega$$

are satisfied for given m.

Fig. 5 shows a typical situation in mesh adaptation for time-dependent problems. This figure shows the value of the interpolation error with respect to the physical time $t \in (0,T)$. In several steps, the interpolation error is over the tolerance ω and therefore a re-meshing (step (S4)) is performed (typically accompanied by the decrease of the size of the time step). The node corresponding to the accepted grids are highlighted.

In the following we present several numerical experiments demonstrating the efficiency of the proposed algorithm. In all numerical experiments we measure the interpolation error in the L^2-norm (i.e., $q = 2$ in Problem 5.1).

6. Numerical verification

6.1. Convergence of an interpolant to the given function

On a unit square $(0,1)\times(0,1)$, we consider the function

$$u(x_1,x_2) = \left(c_1 + c_2(1-x_1) + e^{-x_1/\varepsilon}\right)\left(c_1 + c_2(1-x_2) + e^{-x_2/\varepsilon}\right), \tag{35}$$

where $c_1 = -e^{-1/\varepsilon}$, $c_2 = -1 - c_1$ and $\varepsilon > 0$. This function exhibits two thing boundary layers along the left and the bottom part of the domain. We apply the Algorithm (A) from Section 3.5 and investigate the dependence of the interpolation error $\|u - \Pi_{hp}u\|_{L^2(\Omega)}$ on the prescribed tolerance ω. In virtue of Remark 4.1, we use the value $z = 0.1$.

The results for $\varepsilon = 10^{-2}$ and $\varepsilon = 10^{-3}$ are summarized in Table 1, where $\#\mathcal{T}_{hp}$ denotes the number of triangles of the generated *hp*-grids, N_{hp} the corresponding number of degrees of freedom and EOC means the *experimental order of convergence* evaluated for each pair of consecutive computations such that $\|u - \Pi_{hp}u\|_{L^2} = c(N_{hp})^{\mathrm{EOC}/2}$, where $c > 0$. Furthermore, we evaluate the ratio $\|u - \Pi_{hp}u\|_{L^2}/\omega$ which oscillates (for smaller tolerances ω) over 1 and thus it is more or less independent of ω. This shows the interpolation error is bounded (up to an constant) by the tolerance ω. Finally, Fig. 6 shows the *hp*-grids generated for $\omega = 10^{-7}$, each triangle is highlighted by the colour corresponding to the polynomial approximation degree.

6.2. Interior layer propagation

We consider the nonlinear convection–diffusion (viscous Burgers) equation

$$\frac{\partial u}{\partial t} + u\frac{\partial u}{\partial x_1} + u\frac{\partial u}{\partial x_2} - \varepsilon\Delta u = 0 \quad \text{in} \quad \Omega\times(0,T) \tag{36}$$

with $\Omega = (-1,1)\times(-1,1)$, $T = 1$, $\varepsilon = 10^{-2}$. The initial and boundary condition are chosen in such a way that the exact solution has the form

$$u(x_1,x_2,t) = \left(1 + \exp\left((x_1 + x_2 + 1 - t)/2\varepsilon\right)\right)^{-1}. \tag{37}$$

This function contains an interior layer propagating in the direction $(1,1)$ and its width is proportional to ε. We carried out numerical experiments for piecewise linear and quadratic approximation with respect to the time ($k = 1$ and $k = 2$ in (30)) and with the tolerances $\omega = 10^{-3}$, $\omega = 10^{-4}$ and $\omega = 10^{-5}$.

The results are shown in Table 2, which contains the number of time steps $\#\tau_m$, the number of different *hp*-meshes $\#\mathcal{T}_{hp}^{(m)}$, the maximal used polynomial degree $p_K^{\max}$, the average size of the time step $\overline{\tau}_m$, the minimal, average and maximal number of degree of freedom $N_{hp}^{(m)}$ for all $\mathcal{T}_{hp}^{(m)}$, $m = 0,\ldots,r$, the average and the maximal value of the interpolation error $\|E_1^{(m)}\|_{L^2(\Omega)}$ for

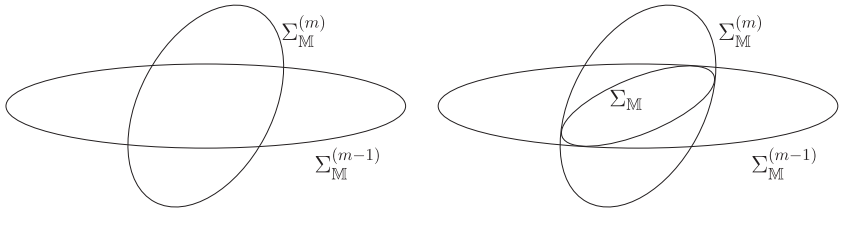

Fig. 4. The ellipses $\Sigma_{\mathbb{M}}^{(m-1)}$ and $\Sigma_{\mathbb{M}}^{(m)}$ corresponding to functions $P_{hp}^{(m)}(u_h)_{m-1}^-$ and $(u_h)_m^-$ at a given node (left) and the corresponding intersection $\Sigma_{\mathbb{M}}$ (right).

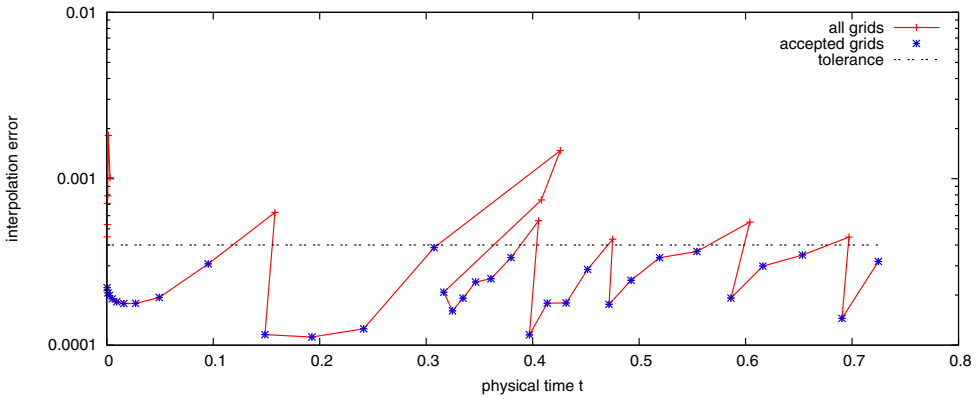

Fig. 5. Typical dependence of the interpolation error with respect to the physical time $t \in (0,T)$ during the adaptation process, the accepted grids are highlighted.

Table 1
Dependence of the interpolation error $\|u - \Pi_{hp}\|_{L^2(\Omega)}$ with respect to ω for u given by (35).

$\varepsilon = 10^{-2}$						$\varepsilon = 10^{-3}$					
ω	$\#\mathcal{T}_{hp}$	$\mathbb{N}_{hp}$	$\|u - \Pi_{hp}u\|_{L^2}$	EOC	$\|u - \Pi_{hp}u\|_{L^2}/\omega$	ω	$\#\mathcal{T}_{hp}$	$\mathbb{N}_{hp}$	$\|u - \Pi_{hp}u\|_{L^2}$	EOC	$\|u - \Pi_{hp}u\|_{L^2}/\omega$
1.0E−02	35	592	1.415E−01	–	1.415E+01	1.0E−02	35	592	1.415E−01	–	1.415E+01
1.0E−03	59	1480	3.814E−03	15.8	3.814E+00	1.0E−03	59	1480	3.814E−03	15.8	3.814E+00
1.0E−04	82	2730	1.845E−04	19.8	1.845E+00	1.0E−04	82	2730	1.845E−04	19.8	1.845E+00
1.0E−05	79	3972	8.660E−06	32.6	8.660E−01	1.0E−05	79	3972	8.660E−06	32.6	8.660E−01
1.0E−06	101	6256	1.180E−06	17.6	1.180E+00	1.0E−06	101	6256	1.180E−06	17.6	1.180E+00
1.0E−07	136	9874	8.515E−08	23.0	8.515E−01	1.0E−07	136	9874	8.515E−08	23.0	8.515E−01

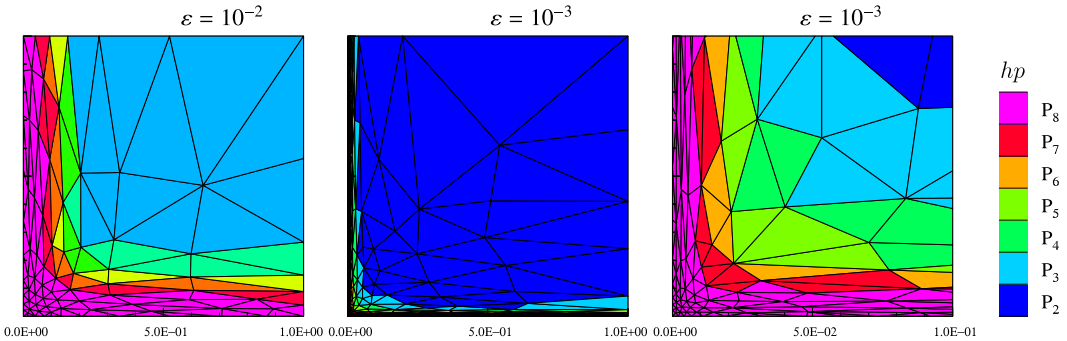

Fig. 6. The hp-grids generated for the function from (35) with $\omega = 10^{-7}$, $\varepsilon = 10^{-2}$ (left) and $\varepsilon = 10^{-3}$ (center) with its detail (right).

$m = 0, \dots, r$, the computational errors measured in the $L^\infty(0,T;L^2(\Omega))$-, $L^2(0,T;L^2(\Omega))$-norms and the $L^2(0,T;H^1(\Omega))$-seminorm and the total computational time in seconds (performed on one Intel core 2.70 GHz in double precision). Let us note that $N_{hp}^{(m)} = \sum_{K \in \mathcal{T}_{hp}^{(m)}} (k+1)(p_K+1)(p_K+2)/2$. Finally, for each pair of consecutive computations we evaluate the *experimental order of convergence* (EOC) according to the relation $\|u - u_h\| = c(N_{hp})^{\mathrm{EOC}/2}$, where $c > 0$.

We observe that all computations fulfil condition $(P1^\star)$ from Problem 5.1 and the ratios

$$\frac{\max_{m=0,\dots,r}\|E_{\mathrm{I}}^{(m)}\|_{L^2(\Omega)}}{\|e_h\|_{L^\infty(0,T;L^2(\Omega))}}, \quad \frac{\max_{m=0,\dots,r}\|E_{\mathrm{I}}^{(m)}\|_{L^2(\Omega)}}{\|e_h\|_{L^2(0,T;L^2(\Omega))}} \quad \text{and} \quad \frac{\max_{m=0,\dots,r}\|E_{\mathrm{I}}^{(m)}\|_{L^2(\Omega)}}{\|e_h\|_{L^2(0,T;H^1(\Omega))}}$$

are practically independent of ω and k. Moreover, comparing results for $k = 1$ and $k = 2$ we find that both give approximately the same computational errors (for the same ω) but the higher order method ($k = 2$) is faster although it employs the higher number of DOF. It is caused by the fact that due to its high accuracy, the time steps can be chosen longer.

Furthermore, Fig. 7 shows the development of the computational error in the $L^2(\Omega)$- and $L^\infty(0,t_m;L^2(\Omega))$-norms and the value of the interpolation error $E_{\mathrm{I}}^{(m)}$ during the computation. We observe that the computational as well as interpolation errors decrease after each re-meshing and each mesh can be employed for several time steps which save the total computational time. This effect is a consequence of the choice of tolerance mentioned in Remark 4.1.

Table 2
Example (36) and (37), characteristics of the mesh adaptation processes and the corresponding computational errors.

k	ω	$\#\tau_m$	$\#\mathcal{T}_{hp}^{(m)}$	$p_K^{\max}$	$\overline{\tau}_m$	$N_{hp}^{(m)}$			$\|\|E_1^{(m)}\|\|_{L^2(\Omega)}$		$\|u-u_h\|$			Comput. time (s)
						Min	Aver	Max	Aver	Max	$L^\infty(L^2)$	$L^2(L^2)$	$L^2(H^1)$	
1	10^{-3}	316	22	4	3.16E−03	786	1214	1706	5.04E−04	9.96E−04	2.98E−03	1.75E−03	1.35E−01	157.9
1	10^{-4}	882	28	5	1.13E−03	1696	2615	6058	5.10E−05	9.98E−05	3.39E−04	1.92E−04	1.57E−02	1004.8
	(EOC)										(5.67)	(5.76)	(5.60)	
1	10^{-5}	3222	37	7	3.10E−04	2458	4420	37026	5.87E−06	1.00E−05	3.73E−05	1.61E−05	1.39E−03	7843.6
	(EOC)										(8.41)	(9.46)	(9.23)	
2	10^{-3}	152	21	4	6.57E−03	1377	1793	2544	3.67E−04	9.90E−04	2.24E−03	1.07E−03	9.19E−02	133.5
2	10^{-4}	239	25	6	4.17E−03	2313	3880	12822	4.15E−05	9.99E−05	2.94E−04	1.41E−04	1.15E−02	621.5
	(EOC)										(5.26)	(5.26)	(5.38)	
2	10^{-5}	429	36	7	2.33E−03	3333	5800	44772	6.21E−06	9.99E−06	2.70E−05	1.29E−05	1.15E−03	2620.6
	(EOC)										(11.86)	(11.87)	(11.45)	

Finally, Fig. 8 shows the anisotropic *hp*-grids generated by the algorithm for $k=2$ with the tolerances $\omega=10^{-3}$ and $\omega=10^{-5}$ at time levels $t=0$, $t=0.5$ and $t=1$. A strong anisotropic refinement along the moving front is obvious.

7. Application to the numerical solution of the compressible Navier–Stokes equations

7.1. Modification of the algorithm

Our aim is to extend the technique introduced in Section 5 to more challenging problems, namely to simulation of viscous compressible flows described by the Navier–Stokes equations. For their form, see, e.g., [37] and for their DG discretization, e.g., [38,34]. These problems are more complicated since they can involve several physical features. A typical example is the shock-vortex interaction presented in Section 7.2. The problem contains the shock wave and an isotropic vortex. The shock wave is (almost) discontinuous and thus a numerical approximation of the corresponding directional derivatives gives very large values. On the other hand, the directional derivatives corresponding to the vortex are significantly smaller. Therefore, a direct application of Algorithm (A) causes (based on the prescribed tolerance) either adaptation only along the shock wave or enormous large number of triangles. Hence, we develop the following *limitation*.

We prescribe the minimal edge of the element $\ell_{\min}$ and require that all edges of all triangles are longer then $\ell_{\min}$. Namely, after the step (d) of Algorithm (A) we perform the following steps:

$$h^\perp := \max(\ell_{\min}, h_E(x)/\sigma_E(x)), \quad h_E(x) := h^\perp \sigma_E(x), \quad x\in\Omega. \tag{38}$$

It means that the aspect ratio σ_E is unchanged in the limitation. Concerning the choice of $\ell_{\min}$ we use the following heuristic consideration. We expect that the numerical capturing of the shock wave should have the width $\approx \mathrm{Re}^{-1}$, where Re is the Reynolds number. Moreover, taking into account that the DG discretization has $p+1$ degrees of freedom in one direction, then we put $\ell_{\min} := (p_E+1)/\mathrm{Re}$, where p_E is the tested polynomial degree in Algorithm (A). Numerical experiments shows that this limitations avoids the drawback mentioned above. Finally, let us not that in order to ensure the convergence of the adaptation algorithm for the time dependent problems, the condition (33) is weaken, namely we replace Ω by $\Omega\setminus\Omega'$, where $\Omega'\subset\Omega$ and Ω' contains elements where the limitation (38) was non-trivially performed.

7.2. Numerical simulation of viscous shock-vortex interaction

Similarly as in [39–41,34], we consider the viscous interaction of a plane weak shock wave with a single isentropic vortex. During the interaction, acoustic waves are produced, and we investigate the ability of the numerical scheme to capture these

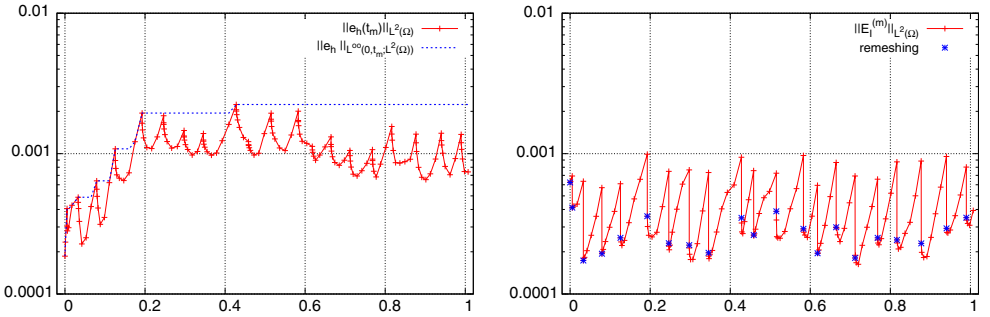

Fig. 7. Example 36,37, $k=2$ and $\omega=10^{-3}$, development of the computational error in the $L^2(\Omega)$- and $L^\infty(0,t_m;L^2(\Omega))$-norms (top) and the value of the interpolation error $E_1^{(m)}$ with respect to the physical time $t\in(0,1)$ (bottom). The highlighted nodes denote re-meshings.

waves. The computational domain is $\Omega = (0,2) \times (0,2)$ with the periodic extension in the x_2-direction. A stationary plane shock wave is located at $x_1 = 1$. The prescribed pressure jump through the shock is $\mathrm{p}_R - \mathrm{p}_L = 0.4$, where p_L and p_R are the pressure values from the left and right of the shock wave, respectively, corresponding to the inlet (left) Mach number $M_L = 1.1588$. The reference density and velocity are those of the free uniform flow at infinity. In particular, we define the initial density, x_1-component of velocity and pressure by

$$\rho_L = 1, \quad u_L = M_L \gamma^{1/2}, \quad \mathrm{p}_L = 1, \quad \rho_R = \rho_L K_1, \quad u_R = u_L K_1^{-1}, \quad \mathrm{p}_R = \mathrm{p}_1 K_2,$$

where

$$K_1 = \frac{\gamma+1}{2} \frac{M_L^2}{1 + \frac{\gamma-1}{2} M_L^2}, \quad K_2 = \frac{2}{\gamma+1} \left(\gamma M_L^2 - \frac{\gamma-1}{2} \right).$$

Here, the subscripts $_L$ and $_R$ denote the quantities at $x < 1$ and $x > 1$, respectively, $\gamma = 1.4$ is the Poisson constant. The Reynolds number is 2000. An isolated isentropic vortex centered at $(0.5, 1)$ is added to the basic flow. The angular velocity in the vortex is given by

$$v_\theta = c_1 r \exp(-c_2 r^2), \quad c_1 = u_c / r_c, \quad c_2 = r_c^{-2}/2, \quad r = \left((x_1 - 0.5)^2 - (x_2 - 1)^2 \right)^{1/2},$$

where we set $r_c = 0.075$ and $u_c = 0.5$. The computations are stopped at the dimensionless time $T = 0.7$.

We solved this problem with the aid of Algorithm (A) with the modification presented in Section 7.1. The density ρ is used as the quantity u in (33) and in condition ($P1^\star$) of Problem 5.1 We carried out the computations with quadratic approximation with respect to the time ($k = 2$ in (30)) and with the tolerances $\omega = 8 \cdot 10^{-4}$, $\omega = 4 \cdot 10^{-4}$, $\omega = 2 \cdot 10^{-4}$ and $\omega = 10^{-4}$.

The results are shown in Table 3, which contains the number of time steps $\#\tau_m$, the number of different hp-meshes $\#\mathcal{T}_{hp}^{(m)}$, the maximal used polynomial degree $p_K^{\max}$, the average size of the time step $\overline{\tau}_m$, the minimal, average and maximal number of

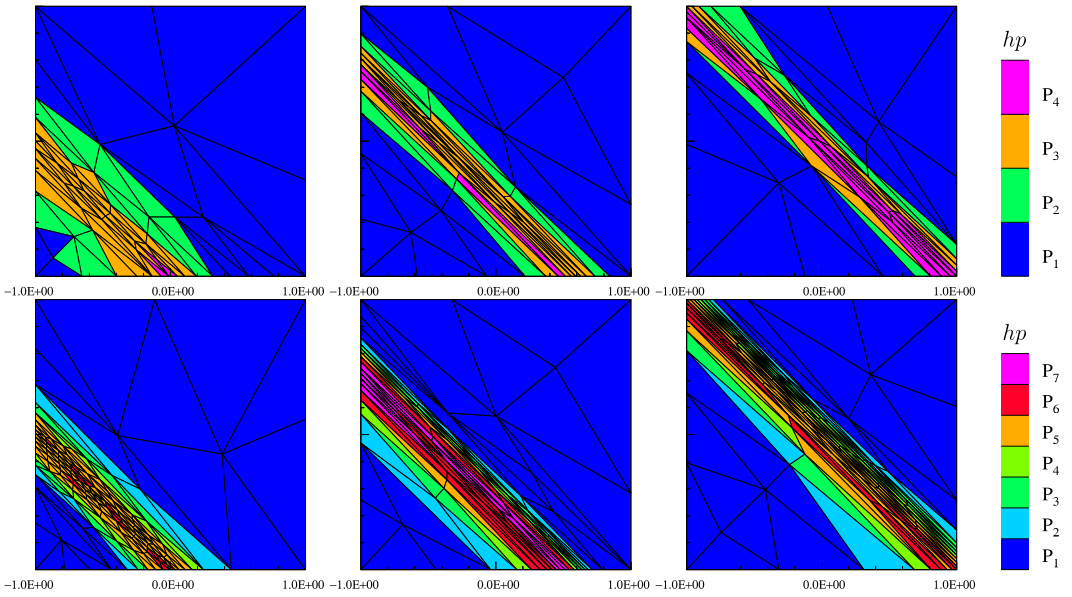

Fig. 8. Example 36,37, $k = 2$, $\omega = 10^{-3}$ (top) and $\omega = 10^{-5}$ (bottom), the hp-grids at $t = 0$ (left), $t = 0.5$ (centre) and $t = 1$ (right).

Table 3
Viscous shock-vortex interaction, characteristics of the mesh adaptation processes and the corresponding interpolation errors.

ω	$\#\tau_m$	$\#\mathcal{T}_{hp}^{(m)}$	$p_K^{\max}$	$\overline{\tau}_m$	$N_{hp}^{(m)}$			$\|E_I^{(m)}\|_{L^2(\Omega)}$		Comput. time (s)
					Min	Aver	Max	Aver	Max	
$8 \cdot 10^{-4}$	16	6	5	4.12E−02	29,076	47,093	69,528	5.48E−04	7.89E−04	1387.2
$4 \cdot 10^{-4}$	31	7	5	2.23E−02	42,816	84,916	101,160	2.21E−04	3.86E−04	3783.1
$2 \cdot 10^{-4}$	30	9	6	2.32E−02	51,024	88,407	105,948	1.33E−04	1.98E−04	4900.1
$1 \cdot 10^{-4}$	37	12	7	1.88E−02	70,536	100,744	122,436	5.58E−05	9.86E−05	8051.1

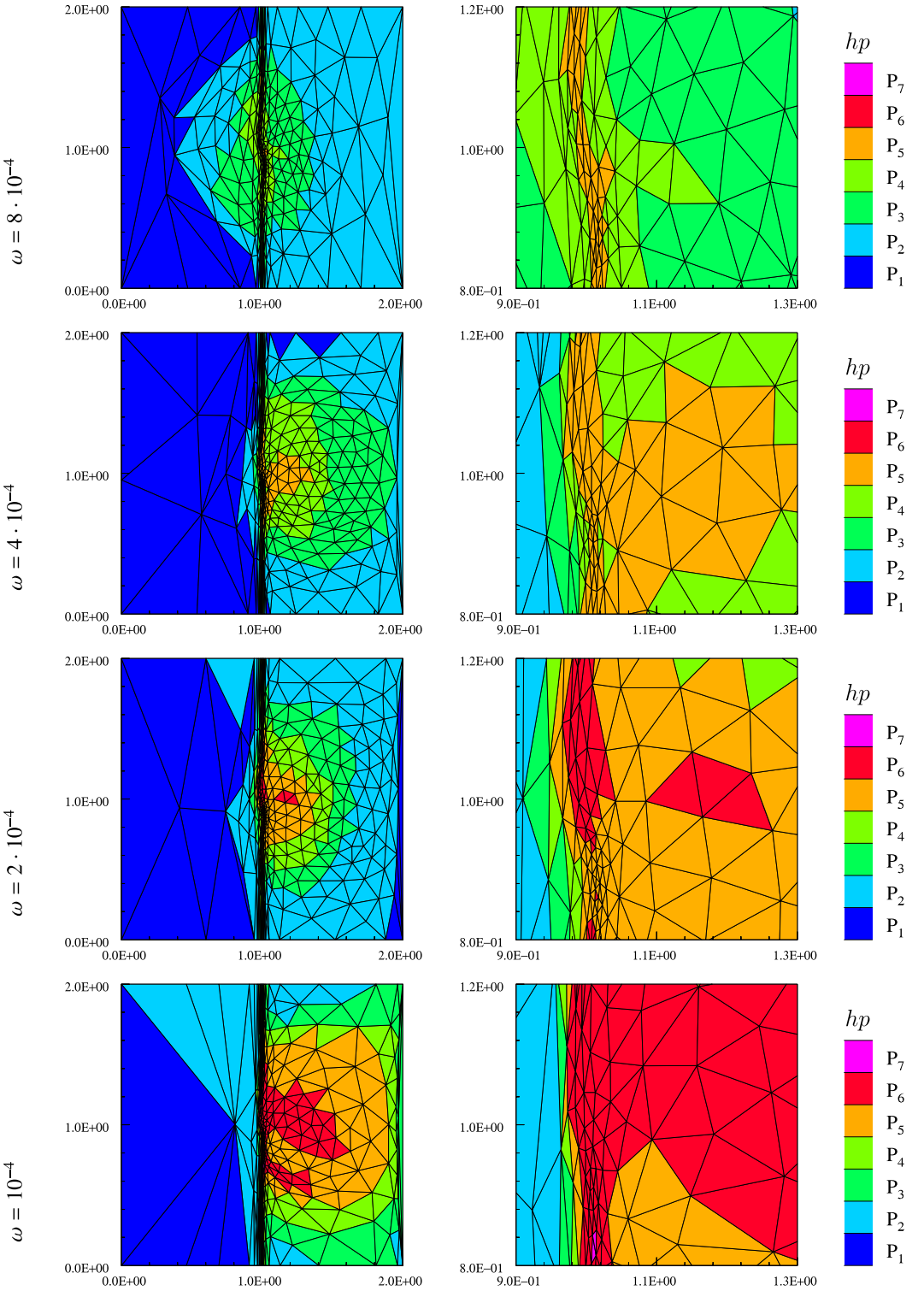

Fig. 9. Viscous shock-vortex interaction: *hp*-grids, total view (left) and a zoom (right).

degree of freedom $N_{hp}^{(m)}$ for all $\mathcal{T}_{hp}^{(m)}$, $m = 0, \ldots, r$, the average and the maximal value of the interpolation error $\|E_I^{(m)}\|_{L^2(\Omega)}$ for $m = 0, \ldots, r$ and the total computational time in seconds. Let us note that $N_{hp}^{(m)} = \sum_{K \in \mathcal{T}_{hp}^{(m)}} 4(k+1)(p_K+1)(p_K+2)/2$. We observe that all computations fulfil condition $(P1^\star)$ from Problem 5.1.

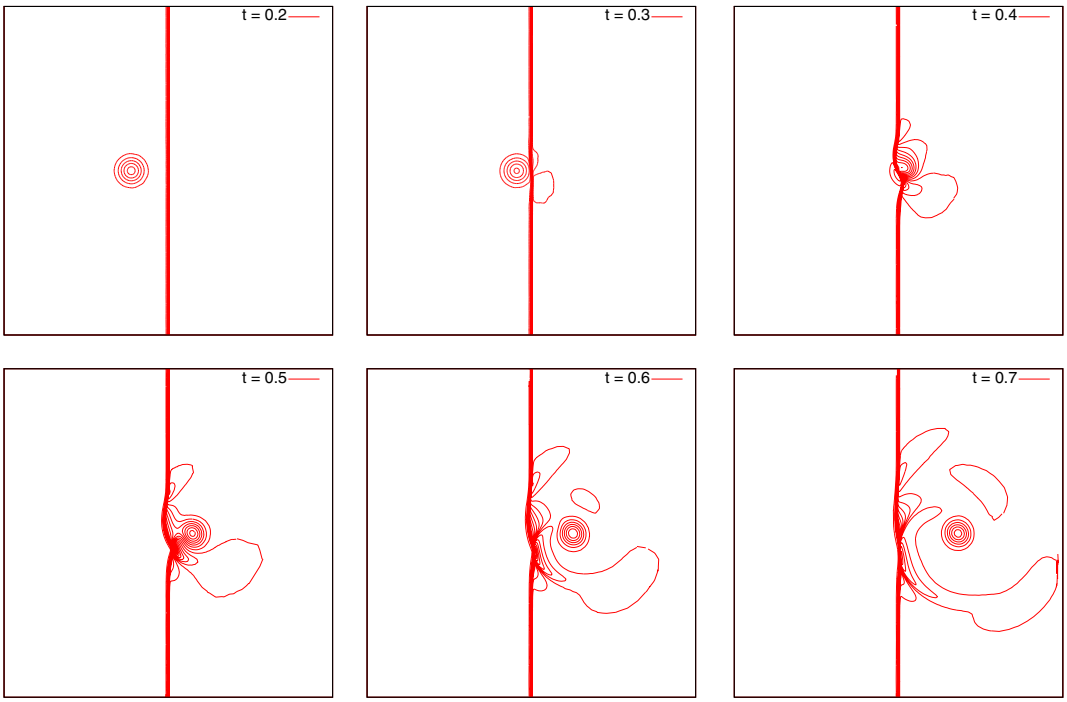

Fig. 10. Viscous shock-vortex interaction: $\omega = 10^{-4}$, pressure isolines at $t = 0.2,\ t = 0.3,\ t = 0.4,\ t = 0.5,\ t = 0.6$ and $t = 0.7$.

Furthermore, Fig. 9 shows the anisotropic *hp*-grids generated by the algorithm for at the final time level $t = 0.7$. Each triangle is highlighted by the colour corresponding to the polynomial approximation degree. A strong anisotropic refinement along the shock wave is obvious. The maximal aspect ratio (stretching) was about 70. Finally, Fig. 10 shows the pressure isolines at several time levels simulating the interaction of the vortex with the stationary shock wave.

8. Conclusion and outlook

We developed the technique for the numerical solution of time dependent partial differential equations, which generates anisotropic *hp*-grids based on the interpolation error estimates in the discrete $L^\infty(0,T;L^q(\Omega))$-norm, $q \in [1,\infty]$. These grids can be employed for the numerical solution with the aid of the space–time discontinuous Galerkin method. Although the presented numerical examples show that the computational error is proportional to the interpolation error estimate (see Table 2), we have not guaranteed error estimate of the computational error. We suppose that it will be possible to combine this approach with some a posteriori error estimation technique. Particularly, we expect that a posteriori error estimate gives us the information about the size of the error and the presented technique about the anisotropy of the elements. This is the subject of the future research.

References

[1] C. Schwab, *p*- and *hp*-Finite Element Methods, Clarendon Press, Oxford, 1998.
[2] J.M. Melenk, *hp*-finite element methods for singular perturbations, Lecture Notes in Mathematics, vol. 1796, Springer-Verlag, Berlin, 1796.
[3] I. Babuška, M. Suri, The *p*- and *hp*-FEM a survey, SIAM Rev. 36 (1994) 578–632.
[4] L. Demkowicz, W. Rachowicz, P. Devloo, A fully automatic *hp*-adaptivity, J. Sci. Comput. 17 (1–4) (2002) 117–142.
[5] P. Šolín, L. Demkowicz, Goal-oriented *hp*-adaptivity for elliptic problems, Comput. Methods Appl. Mech. Eng. 193 (2004) 449–468.
[6] P. Houston, E. Süli, A note on the design of *hp*-adaptive finite element methods for elliptic partial differential equations, Comput. Methods Appl. Mech. Eng. 194 (2005) 229–243.
[7] D. Ait-Ali-Yahia, G. Baruzzi, W.G. Habashi, M. Fortin, J. Dompierre, M. Vallet, Anisotropic mesh adaptation: towards user-independent, mesh-independent and solver-independent CFD. II: Structured grids, Int. J. Numer. Methods Fluids 39 (2002) 657–673.
[8] R. Aubry, R. Löhner, Generation of viscous grids at ridges and corners, Int. J. Numer. Methods Eng. 77 (9) (2009) 1247–1289.
[9] V. Dolejší, Anisotropic mesh adaptation for finite volume and finite element methods on triangular meshes, Comput. Vis. Sci. 1 (3) (1998) 165–178.
[10] V. Dolejší, J. Felcman, Anisotropic mesh adaptation and its application for scalar diffusion equations, Numer. Methods Partial Differ. Equ. 20 (2004) 576–608.
[11] J. Dompierre, M.-G. Vallet, Y. Bourgault, M. Fortin, W.G. Habashi, Anisotropic mesh adaptation: towards user-independent, mesh-independent and solver-independent CFD. Part III: Unstructured meshes, Int. J. Numer. Methods Fluids 39 (8) (2002) 675–702.
[12] P.J. Frey, F. Alauzet, Anisotropic mesh adaptation for CFD computations, Comput. Methods Appl. Mech. Eng. 194 (2005) 5068–5082.
[13] W.G. Habashi, J. Dompierre, Y. Bourgault, D. Ait-Ali-Yahia, M. Fortin, M.-G. Vallet, Anisotropic mesh adaptation: towards user-independent, mesh-independent and solver-independent CFD. Part I: General principles, Int. J. Numer. Methods Fluids 32 (6) (2000) 725–744.

[14] A. Loseille, R. Löhner, Boundary layer mesh generation and adaptivity, in: 49th AIAA Aerospace Sciences Meeting including the New Horizons Forum and Aerospace Exposition, 2011.
[15] R.B. Simpson, Anisotropic mesh transformations and optimal error control, Appl. Numer. Math. 14 (1994) 183–198.
[16] O.C. Zienkiewicz, J. Wu, Automatic directional refinement in adaptive analysis of compressible flows, Int. J. Numer. Methods Eng. 37 (13) (1994) 2189–2210.
[17] W. Cao, Anisotropic measures of third order derivatives and the quadratic interpolation error on triangular elements, SIAM J. Sci. Comput. 29 (2) (2007) 756–781.
[18] W. Cao, An interpolation error estimate in R^2 based on the anisotropic measures of higher order derivatives, Math. Comput. 77 (261) (2008) 265–286.
[19] J.-M. Mirebeau, Optimal meshes for finite elements of arbitrary order, Constr. Approx. 32 (2) (2010) 339–383.
[20] J.-M. Mirebeau, Optimally adapted meshes for finite elements of arbitrary order and $W^{1,p}$ norms, Numer. Math. 120 (2) (2012) 271–305.
[21] V. Dolejší, Anisotropic *hp*-adaptive method based on interpolation error estimates in the L^q-norm, Appl. Numer. Math. 82 (2014) 80–114.
[22] D. Guégan, O. Allain, A. Dervieux, F. Alauzet, An L^∞-L^p mesh-adaptive method for computing unsteady bi-fluid flows, Int. J. Numer. Methods Eng. 84 (11) (2010) 1376–1406.
[23] A. Loseille, F. Alauzet, Continuous mesh framework. Part I: Well-posed continuous interpolation error, SIAM J. Numer. Anal. 49 (1) (2011) 38–60.
[24] A. Loseille, F. Alauzet, Continuous mesh framework. Part II: Validations and applications, SIAM J. Numer. Anal. 49 (1) (2011) 61–86.
[25] V. Dolejší, ANGENER – software package, Charles University Prague, Faculty of Mathematics and Physics, 2000, <www.karlin.mff.cuni.cz/dolejsi/angen.html>.
[26] P. Laug, H. Borouchaki, BL2D-V2: isotropic or anisotropic 2D mesher, INRIA, 2002, <https://www.rocq.inria.fr/gamma/Patrick.Laug/logiciels/bl2d-v2/INDEX.html>.
[27] V. Thomée, Galerkin Finite Element Methods for Parabolic Problems, second revised and expanded ed., Springer, Berlin, 2006.
[28] G. Akrivis, C. Makridakis, Galerkin time-stepping methods for nonlinear parabolic equations, ESAIM: Math. Model. Numer. Anal. 38 (2004) 261–289.
[29] K. Chrysafinos, N.J. Walkington, Error estimates for the discontinuous Galerkin methods for parabolic equations, SIAM J. Numer. Anal. 44 (2006) 349–366.
[30] K. Eriksson, C. Johnson, Adaptive finite element methods for parabolic problems. I: A linear model problem, SIAM J. Numer. Anal. 28 (1) (1991) 43–77.
[31] D. Schötzau, C. Schwab, An hp a priori error analysis of the discontinuous Galerkin time-stepping for initial value problems, Calcolo 37 (2000) 207–232.
[32] J. Česenek, M. Feistauer, Theory of the space-time discontinuous Galerkin method for nonstationary parabolic problems with nonlinear convection and diffusion, SIAM J. Numer. Anal. 30 (2012) 1181–1206.
[33] M. Feistauer, V. Kučera, K. Najzar, J. Prokopová, Analysis of space–time discontinuous Galerkin method for nonlinear convection–diffusion problems, Numer. Math. 117 (2011) 251–288.
[34] V. Dolejší, A design of residual error estimates for a high order BDF-DGFE method applied to compressible flows, Int. J. Numer. Methods Fluids 73 (6) (2013) 523–559.
[35] V. Dolejší, F. Roskovec, M. Vlasák, Residual based error estimates for the space-time discontinuous Galerkin method applied to the compressible flows, Comput. Fluids.
[36] V. Dolejší, Anisotropic mesh adaptation technique for viscous flow simulation, East–West J. Numer. Math. 9 (1) (2001) 1–24.
[37] M. Feistauer, J. Felcman, I. Straškraba, Mathematical and Computational Methods for Compressible Flow, Oxford University Press, Oxford, 2003.
[38] V. Dolejší, M. Holík, J. Hozman, Efficient solution strategy for the semi-implicit discontinuous Galerkin discretization of the Navier–Stokes equations, J. Comput. Phys. 230 (2011) 4176–4200.
[39] V. Daru, C. Tenaud, High order one-step monotonicity-preserving schemes for unsteady compressible flow calculations, J. Comput. Phys. 193 (2) (2004) 563–594.
[40] J. Fürst, Modélisation numérique d'écoulements transsoniques avec des schémas TVD et ENO (Ph.D. thesis), Universite Mediterranee, Marseille and Czech Technical University Prague, 2001.
[41] C. Tenaud, E. Garnier, P. Sagaut, Evaluation of some high-order shock capturing schemes for direct numerical simulation of unsteady two-dimensional free flows, Int. J. Numer. Methods Fluids 126 (2000) 202–228.